INTERNATIONAL JOURNAL FOR NUMERICAL METHODS IN FLUIDS
*Int. J. Numer. Meth. Fluids* 2001; **35**: 533–557

# Numerical solution of three-dimensional Navier–Stokes equations by a velocity–vorticity method

Chung Ho Liu*,[1]

*Rotating Fluids and Vortex Dynamics Laboratory, Department of Aeronautical Engineering, Chung Cheng Institute of Technology, Tahsi, Taoyuan, Taiwan, Republic of China*

## SUMMARY

A finite difference method for solving the incompressible viscous flow in velocity–vorticity form is presented. A staggered mesh is employed to ensure continuity. To enforce the zero divergence of the vorticity, the computed vorticity is replaced at each time step with $\nabla \wedge \vec{u}$. An explicit three-level backward scheme is used to update the vorticity transport equation for the vorticity at the next time level. To solve the Poisson equations for velocity, a restarted version of the Generalized Minimal Residual method (GMRES) implemented with incomplete lower–upper (ILU) decompositions preconditioner has been adopted. Two- and three-dimensional driven cavity flows with impulsively started and oscillating lids are used to test the method. Detailed results and comparisons with the numerical literature data show that the proposed method is accurate and efficient. Copyright © 2001 John Wiley & Sons, Ltd.

KEY WORDS: incompressible flow; lid-driven flow; preconditioned GMRES method; velocity–vorticity formulation

## 1. INTRODUCTION

Most numerical simulations for the solution of three-dimensional Navier–Stokes equations are usually expressed in the primitive variables [1] (velocity–pressure), vector potential–vorticity [2] and velocity–vorticity [3] formulations. The peculiarities of the three formulations are reviewed in Gresho [4]. Generally, the formulation of primitive variables is widely employed, but difficulties occur with the pressure boundary conditions. The latter two formulations have a distinct advantage since the pressure does not appear in the field equations. For the vector potential–vorticity method, the vector potential is not uniquely defined and it is necessary to introduce a scalar potential for the through-flow problems. However, the velocity–vorticity formulation presents a relatively easier treatment of the boundary conditions and also offers some advantages with respect to the primitive variable approach [5].

* Correspondence to: Department of Aeronautical Engineering, Chung Cheng Institute of Technology, Tahsi, Taoyuan, Taiwan 335, Republic of China.
[1] E-mail: chliu@ccit.edu.tw

*Received May 1999*
*Revised February 2000*

For the velocity–vorticity formulations, the set of equations to be solved always includes a vorticity transport equation. The remaining equations can be written in two forms. In the first approach, the additional equations to be solved include the continuity and the definition of the vorticity as the curl of velocity. Given appropriate initial and boundary conditions, these can be used to solve for velocity and vorticity. Gatski *et al.* [6] have developed a two-dimensional form of these equations and have used this two-dimensional version of the algorithm in a study of surface drag effects over an embedded cavity [7]. Later, they extended the two-dimensional version to three dimensions [8].

In the second approach, the remaining equations are three Poisson equations for each component of the velocity vector. This approach is more straightforward because the coupled equations for the velocity and vorticity can be solved simultaneously at each grid point. An early use of this was in the study of the stability of two-dimensional boundary layers by Fasel [9]. The work has been extended to study the three-dimensional development of disturbances in a spatially growing boundary layer [10]. Dennis *et al.* [11] used a finite difference method to solve the steady three-dimensional Navier–Stokes equations. The flow inside a cubical box with an impulsively started lid was studied for Reynolds numbers up to 100.

Farouk and Fusegi [12] studied the nature and forced convection in both a square cavity and a horizontal circular annulus. Orlandi [13] used an implicit time step scheme and a staggered mesh, which coupled the field equations and boundary conditions, to solve the two-dimensional driven cavity and backward-facing step problems. Guj and Stella [3,14] used this formulation to solve two- and three-dimensional incompressible flows. Ern and Smooke [15] studied three-dimensional steady compressible fluid flow and heat transfer problems. Yuan *et al.* [16] studied the axisymmetric unsteady spherical Couette flow at moderate Reynolds number. At each stage a vector Poisson equation for velocity is solved. The solution is advanced in time with an explicit two-stage Runge–Kutta method. For an implicit method, Stella and Bucchignani [17] used a preconditioned bi-conjugate gradient algorithm (Bi-CGATAB) to solve the heat transfer problems. A diagonal scaling and the classical incomplete lower–upper (ILU) decompositions are chosen as the preconditioner. More recently, Huang and Li [18] and Pascazio and Napolitano [19] also used this algorithm to solve the two-dimensional incompressible flow problems. Shen and Loc [20] solved three-dimensional unsteady problems using the same algorithm.

Among the previous approaches, most of the researchers adopted conservative forms of the vorticity transport equation and solved the remaining equations by finite difference, finite element or spectral methods, usually with a fixed Eulerian grid. The approach that uses non-conservative form of the vorticity transport equation has received less attention. Expressing vorticity transport equation in conservative form is advantageous, since with consistent discretization it is readily shown that an initial solenoidal vorticity field should remain so. In this paper, however, the non-conservative form is used. This interest is due to the convective term of the vorticity transport equation, which can be easily substituted by the vortex particle-in-cell method [23,24]. Therefore, the numerical instability caused by the convective term can be avoided. This research may serve as a base for further studies on three-dimensional vortex particle-in-cell methods.

In this paper an alternative velocity–vorticity formulation, using a non-conservative form of the vorticity transport equation, is proposed. The problem that arises when using this

 

approach is the satisfaction of the divergence constraint on the velocity and vorticity. There are a number of possibilities to approach the problem of solenoidality. One of the methods is to solve a Poisson equation for a suitably chosen scalar potential on a staggered mesh. In presenting the method developed here, all variables of the scheme are located on a staggered grid and the solution update is explicit by a three-level backward scheme, continuity can be satisfied to machine accuracy. The soleniodality of vorticity is enforced simply by substituting for $\vec{\omega}$ directly from $\nabla \wedge \vec{u}$. This is more economical than the solution of a scalar potential for three-dimensional computations [8]. For solving the Poisson equations of velocity, a restarted version of the Generalized Minimal Residual method (GMRES) with ILU preconditioner has been adopted. Two- and three-dimensional driven cavity flows with impulsively started or oscillating lids are chosen to test the method. Detailed results and comparisons with the numerical literature are presented.

## 2. THE GOVERNING EQUATIONS

The non-dimensional Navier–Stokes equations for incompressible Newtonian fluid can be written in terms of vorticity and velocity by taking the curl of the momentum equations and taking into account the continuity equation, thus eliminating the pressure term from the formulation. This leads to the transport equation for vorticity. In order to close the system of equations, the continuity and the vorticity definitions are needed. Therefore, the governing equations are summarized as

$$\frac{\partial \vec{\omega}}{\partial t} + \vec{u} \cdot \nabla \vec{\omega} = \vec{\omega} \cdot \nabla \vec{u} + \frac{\nabla^2 \vec{\omega}}{Re}, \quad \text{in } D \tag{1}$$

$$\vec{\omega} = \nabla \wedge \vec{u} \quad \text{in } D \tag{2}$$

$$\nabla \cdot \vec{u} = 0 \quad \text{in } D \tag{3}$$

$$\vec{u} = \vec{u}_\Gamma \quad \text{on } \Gamma = \partial D \tag{4}$$

where $D$ is the computational domain with the boundary $\Gamma = \partial D$. To solve Cauchy–Riemann relations (2) and (3), Gatski *et al.* [8] explicitly use a least-squares solution of the overdetermined system of Equations (2) and (3) to yield the velocity field for a known vorticity. The vorticity transport equation then updates vorticity, and the vorticity is rendered divergence-free by obtaining the Helmholtz projection.

Alternatively, a vector Poisson equation can be used to relate the velocity and vorticity field [13–21]

$$\nabla^2 \vec{u} = -\nabla \wedge \vec{\omega} \tag{5}$$

Equations (2) and (3) are replaced by an alternative system of equations, comprising Equations (1), (2) and (5). In Reference [23] we have shown that the system of Equations (1)–(4) is

 

equivalent to the Equations (1), (2) and (5). To determine the solution of Equations (1), (2) and (5), the boundary velocity ($\vec{u}|_b$) and vorticity ($\vec{\omega}|_b$) must be specified. Without further compatability conditions, however, there is no guarantee that the solution satisfies either $\nabla\cdot\vec{u}=0$ or $\vec{\omega}=\nabla\wedge\vec{u}$ with $\vec{\omega}$ representing the computed vorticity. However, following Daube [21], enforcing Equation (2) at the boundary ensures that both of the above conditions hold in the two-dimensional case. In the three-dimensional case it is also necessary to ensure that $\vec{\omega}$ is solenoidal, i.e. $\nabla\cdot\vec{\omega}=0$. This means that the Poisson equation (5) with velocity boundary conditions cannot ensure a solenoidal velocity field for an arbitrary vorticity distribution. In the following section, we will develop a numerical method based on the system of Equations (1), (2) and (5), which satisfies the zero divergence of the vorticity field and its correct relationship to the velocity.

## 3. ENFORCING CONTINUITY EQUATION

Daube [21] considered an explicit treatment for the convection and an implicit treatment for the diffusion, and shows that $\nabla\cdot\vec{u}=0$ may be assured by proper specification of vorticity on the boundary. Specifically, he showed that provided the values of boundary vorticity are chosen such that the curl of velocity is equal to the vorticity there, the computed velocity field has zero divergence. Since it is not possible *a priori* to chose values of vorticity that achieve this, an estimated solution is first obtained with a guessed value for the boundary vorticity. An influence matrix can be constructed from the homogenous problem that relates the velocity field within the domain to the vorticity at each individual boundary point. Hence, a linear combination of the estimated solution and that of the influence problem can be found such that the vorticity on the boundary is consistent with the computed velocity field there. In previous work [23], it can be readily shown that provided a consistent differencing is used (readily accomplished on a staggered mesh), and the solution update is explicit, continuity can be satisfied to machine accuracy without requiring the solution of an influence matrix. However, in extending this to the three-dimensional case, it is further necessary to ensure the divergence of vorticity is constrained to zero in the updating procedure. Therefore, if we can enforce the constraint $\nabla\cdot\vec{\omega}=0$ in the domain $D$, the continuity equation can then be automatically satisfied.

## 4. ENFORCING ZERO DIVERGENCE OF VORTICITY FIELD IN THE THREE-DIMENSIONAL CASE

The solenoidality of the vorticity is satisfied for two-dimensional problems because of the orthogonality between the vorticity vector and the plane of motion. In three-dimensional problems, the solenoidality of the vorticity is not guaranteed explicitly, so that the condition has to be explicitly enforced.

For the set of equations used in the present work, we compute the new vorticity field $\vec{\omega}$ from the vorticity transport equation. There will be errors due to numerical inaccuracy, and it is not guaranteed that the computed vorticity will satisfy $\nabla\cdot\vec{\omega}=0$. Nor is it assured that the curl of

 

the calculated velocity field, which we denote by $\vec{\zeta}$, will correspond exactly to $\vec{\omega}$. However, provided that we correct the computed vorticity so that it has zero divergence, in such a way that the velocity field is unchanged, then by the vector identity

$$\nabla(\nabla\cdot\vec{u}) - \nabla\wedge(\nabla\wedge\vec{u}) = -\nabla\wedge\vec{\omega} \tag{6}$$

the continuity equation for velocity will be satisfied.

There are a number of possibilities to update the vorticity, but the simplest are (i) to replace the vorticity $\vec{\omega}$ with $\nabla\wedge\vec{u}$ by direct substitution or (ii) to take the Helmholtz projection of $\vec{\omega}$.

In (i), using the same notation as before, if we assume $\vec{\varepsilon} = \vec{\zeta} - \vec{\omega}$, then

$$\nabla^2\vec{\varepsilon} = -\nabla(\nabla\cdot\vec{\omega}) \tag{7}$$

can be solved for $\vec{\varepsilon}$, but it is clearly simpler to substitute $\vec{\zeta}$ for $\vec{\omega}$ directly by overwriting $\vec{\omega}$ by $\nabla\wedge\vec{u}$. Alternatively with (ii), if we assume the error in the computed vorticity can be represented as the potential of a scalar function $\phi$, i.e.

$$\vec{\omega}_{\text{true}} = \vec{\omega} + \nabla\phi \tag{8}$$

then

$$\nabla\cdot\vec{\omega}_{\text{true}} = \nabla\cdot\vec{\omega} + \nabla^2\phi$$

or

$$\nabla^2\phi = -\nabla\cdot\vec{\omega} \tag{9}$$

Correcting the vorticity field using Equation (8) does not affect the velocity field, since the right-hand side of the velocity Poisson equation is unchanged. Likewise, this is the case for the direct substitution, but this relies on the boundary conditions excluding solutions with $(\vec{\zeta} - \vec{\omega})$ and not being equal to zero.

The above analysis is based on the continuum equations and the differential operator identities are not necessarily satisfied by the finite difference equations for an arbitrary discretization. For a staggered mesh system, however, the difference equations exactly replicate the various continuum vector identities. Therefore, in setting the wall vorticity condition in our fully explicit scheme, it is possible to ensure that in Equation (5) the differencing of the Laplacian is exactly compatible with the differencing of the right-hand side. Hence, the value of the wall vorticity is in a sense arbitrary for the Poisson solution, which solves for the velocity field corresponding to the new interior vorticity field. The wall vorticity can then be prescribed so that it is compatible with $\vec{u} = 0$ on the wall and $\vec{u} = \vec{u}^{n+1}$ in $D$. As before, the solenoidality of vorticity is enforced by replacing the vorticity at the end of each time step with the curl of the velocity field.

 

### 4.1. Wall boundary conditions

The generation of wall vorticity has proved troublesome for velocity–vorticity formulations in general, due to the lack of boundary conditions on vorticity. For the velocity–Poisson approach considered herein, Daube [21] has shown in the two-dimensional case that appropriate Dirichlet boundary conditions on vorticity may be recovered by using an influence matrix that links the vorticity at the boundary to the satisfaction of continuity within the domain. Daube's discrete analysis for Dirichlet vorticity conditions extends that of Cottet [22] and shows that the influence matrix may be derived by forcing the vorticity to equal the curl of the velocity field on the boundary.

Here we do not attempt an implicit update of the vorticity field. Thus, an explicit Euler step is used to update Equation (1) for the vorticity at the next time level. The corresponding interior velocity field is then found from Equation (5) assuming $\vec{\omega}|_{\mathrm{b}} = 0$ on any no-slip boundaries, i.e. with a homogeneous Neumann velocity condition on tangential surface boundaries. Finally, $\vec{\omega}^{n+1}|_{\mathrm{b}}$ is prescribed so that the slip velocity is zero.

## 5. NUMERICAL IMPLEMENTATION

In the present work, the governing equations are discretized by a finite difference approximation with a uniform mesh in Cartesian co-ordinates using a three-point second-order backward differences for temporal derivatives and standard second-order central differences for the spatial derivatives.

The main features of the scheme are summarized as follows:

- All the variables of the scheme are placed on a staggered mesh to satisfy the zero divergence of the velocity field, but the vorticity field will not be necessarily divergence free, nor equal to the curl of the velocity.
- The solenoidality of vorticity field is enforced by replacing vorticity $\vec{\omega}$ with $\nabla \wedge \vec{u}$.
- The non-conservative form is adopted for the vorticity transport equation. Therefore, the convective term in the vorticity transport equation can be substituted easily by the vortex particle-in-cell method [24] of semi-Lagrangian convective transport.
- The Poisson equation for each component of velocity is solved by the preconditioned GMRES method.

The computational domain is rectangular and is divided into $L \times M \times N$ regular meshes. The locations of the variables on the staggered mesh are shown in Figure 1. In the three-dimensional case, the velocity field for three components $u_x$, $u_y$, $u_z$ are evaluated at the centres of the faces of the computational cell, which is perpendicular to the same axes, and the vorticity field for the three components $\omega_x$, $\omega_y$, $\omega_z$ are evaluated at the centres of the edges parallel to the corresponding axis. Thus, we can summarize the location of the variables as follows. The velocity component $u_x$, $u_y$, $u_z$ are evaluated at nodes $(i, j+1/2, k+1/2)$, $(i+1/2, j, k+1/2)$, $(i+1/2, j+1/2, k)$ respectively. The vorticity components $\omega_x$, $\omega_y$, $\omega_z$ are evaluated at nodes $(i+1/2, j, k)$, $(i, j+1/2, k)$, $(i, j, k+1/2)$ respectively.

 

### 5.1. Vorticity transport equation

The unsteady term in Equation (1) is discretized with a three-level second-order backward scheme

$$\left(\frac{\partial \vec{\omega}}{\partial t}\right)_{i,j,k} = \frac{3\vec{\omega}^{n}_{i,j,k} - 4\vec{\omega}^{n-1}_{i,j,k} + \vec{\omega}^{n-2}_{i,j,k}}{2\Delta t} \tag{10}$$

The quadratic upstream interpolation for convection kinematics (QUICK) [25] scheme is applied to treat the convection term in Equation (1), while the spatial derivative terms of transport equation are discretized using the second-order central difference. For the first time step, the first-order forward difference is employed.

### 5.2. Vorticity boundary conditions

At a solid boundary the vorticity has to be calculated by using the vorticity definition (i.e. curl(velocity)). For instance, at the bottom surface shown in Figure 1, corresponding to $z = 0$

$$\omega_x = -\frac{\partial u_y}{\partial z} = -\frac{u_y(i,j,1/2) - u_y(i,j,-1/2)}{\Delta z} \tag{11}$$

$$\omega_y = \frac{\partial u_x}{\partial z} = \frac{u_x(i,j,1/2) - u_x(i,j,-1/2)}{\Delta z}$$

$$\omega_z = 0 \tag{13}$$

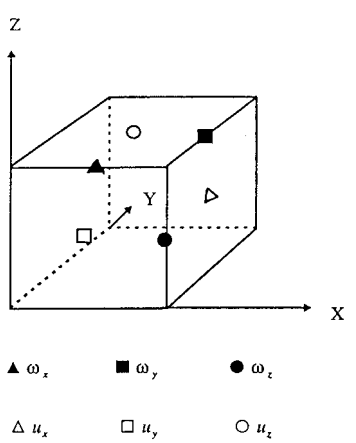


Figure 1. Three-dimensional staggered mesh, showing location of field variables.

 

The value of the velocity at the point $(i, j, -1/2)$, which lies outside the domain, is calculated by the extrapolation [26]

$$\vec{u}(i, j, -1/2) = \frac{\vec{u}(i, j, 3/2) - 6\vec{u}(i, j, 1/2) + 8\vec{u}(i, j, 0)}{3} \tag{14}$$

Therefore, the vorticity boundary conditions at the bottom surface are as follows:

$$\omega_x = \frac{-u_y(i, j, 3/2) + 9u_y(i, j, 1/2)}{3\Delta z} \tag{15}$$

$$\omega_y = \frac{u_x(i, j, 3/2) - 9u_x(i, j, 1/2)}{3\Delta z} \tag{16}$$

$$\omega_z = 0 \tag{17}$$

since $\vec{u}(i, j, 0) = 0$ on the wall surface.

### 5.3. Solution of the Poisson equations

The Poisson equations of the velocity are solved by a restarted version of GMRES(m) [27]. ILU factorizations [28] are used for preconditioning with scaling by the main diagonal pivots of the preconditioner, and the Eisenstat procedure [29] is used to compute the preconditioned matrix–vector multiplication. The Krylov subspace algorithm is an effective iterative method for solving large sparse non-symmetric problems and has an optimal rate of convergence. The discretization of the Poisson equations leads to a large system of equations of the form

$$\boldsymbol{A}\boldsymbol{x} = \boldsymbol{b} \tag{18}$$

where $\boldsymbol{x}$ is the unknown vector and $\boldsymbol{b}$ is the known vector. To solve this linear system, a variant of the preconditioned GMRES is proposed. In the algorithm the two-norm of the residual at each iteration step is minimized. An orthonormal basis generated by the Arnoldi process and the Hessenberg least squares problem can be solved by Householder transformations.

## 6. RESULTS OF TEST PROBLEMS

In this section we present results of testing the numerical method described in the previous section. To validate the present numerical method, a mesh experiment was performed before the course of computations. We propose a model problem to evaluate the accuracy and rate of convergence of the method. An incompressible viscous fluid in two- and three-dimensional cavity flow at various Reynolds numbers has been conducted to serve as a comparison against other already tested numerical methods.

 

### 6.1. Mesh sensitivity and convergence

For the first test case, Navier–Stokes equations were solved on the unit cubic cavity with a uniform mesh. We take the problem that solved the time-dependent vortex spin-up used by Gatski *et al.* [8] and others to test their methods. The exact solution is given by

$$u_r = -\left(\frac{2k^2}{Re}\right)r$$

$$u_\theta = (k^2 R_0 r)^{-1}\left[1 - \exp\left(\frac{-k^2 r^2}{F(t)}\right)\right]$$

$$u_z = \left(\frac{4k^2}{Re}\right)z$$

$$\omega_r = 0$$

$$\omega_\theta = 0$$

$$\omega_z = \frac{2}{F(t)}\exp\left(\frac{-k^2 r^2}{F(t)}\right)$$

where $k = 1.12$, $R_0$ is a Rossby number and $F(t) = 1 + b\exp(-4k^2/Re)$, with $b$ an arbitrary constant. The case of $Re = 100$ and $R_0 = 0.7$ is selected in the computation. The results of mesh sensitivity analysis at $t = 5$ are presented in Table I, where the relative errors are measured in the $L_2$-norm. The order of accuracy given in the table is computed via the formula

$$\alpha = \ln\left[\frac{\mathrm{err}(h_1)}{\mathrm{err}(h_2)}\right] \Big/ \ln\left(\frac{h_1}{h_2}\right)$$

using two successive values of the grid spacing and the corresponding errors. The results give in Table I clearly show the second-order accuracy of the method. Overall, we can observe that the errors for velocity and vorticity decrease with $h^2$. In Table II we list the relative errors for various time steps at mesh spacing 1/20. The convergence analysis based on the data presented in Table II is around 1.9, which means the order of the convergence is approximately second-order.

Table I. Mesh sensitivity analysis for test problem.

| Grid spacing | Err $u_x$ | Order $u_x$ | Err $u_y$ | Order $u_y$ | Err $u_z$ | Order $u_z$ | Err $\omega_z$ | Order $\omega_z$ |
|---|---|---|---|---|---|---|---|---|
| 1/10 | 3.682e−4 | | 3.663e−4 | | 4.152e−4 | | 9.318e−4 | |
| 1/20 | 9.270e−5 | 1.99 | 9.221e−5 | 1.99 | 1.038e−4 | 2.0 | 2.378e−4 | 1.97 |
| 1/30 | 4.103e−5 | 2.01 | 4.082e−5 | 2.01 | 4.650e−5 | 1.98 | 1.065e−4 | 1.98 |
| 1/40 | 2.295e−5 | 2.02 | 2.283e−5 | 2.02 | 2.616e−5 | 2.0 | 5.990e−5 | 2.0 |

Table II. Relative errors and convergence rate for test problem.

| $\Delta t$ | Err $u_x$ | Order $u_x$ | Err $u_y$ | Order $u_y$ | Err $u_z$ | Order $u_z$ | Err $\omega_z$ | Oder $\omega_z$ |
|---|---|---|---|---|---|---|---|---|
| 1/10 | 1.213e−3 | | 1.221e−3 | | 1.875e−3 | | 3.315e3 | |
| 1/20 | 3.228e−4 | 1.9 | 3.249e−4 | 1.9 | 5.024e−4 | 1.89 | 8.882e−4 | 1.9 |
| 1/30 | 1.500e−4 | 1.91 | 1.510e−4 | 1.91 | 2.325e−4 | 1.9 | 4.195e−4 | 1.9 |
| 1/40 | 8.684e−5 | 1.91 | 8.742e−5 | 1.91 | 1.365e−4 | 1.9 | 2.450e−4 | 1.9 |

Table III. Comparison of some characteristic values of the cavity flow.

| | $Re = 100$ | | | $Re = 1000$ | | |
|---|---|---|---|---|---|---|
| | Present paper | Reference [30] | Reference [31] | Present paper | Reference [30] | Reference [31] |
| $ux_{\max}$ | 0.2134 | 0.2109 | 0.2140 | 0.3845 | 0.3829 | 0.3886 |
| $z_{\max}$ | 0.4569 | 0.4531 | 0.4581 | 0.1717 | 0.1719 | 0.1717 |
| $uz_{\max}$ | 0.1787 | 0.1753 | 0.1796 | 0.3731 | 0.3710 | 0.3770 |
| $x_{\max}$ | 0.7627 | 0.7656 | 0.7630 | 0.8424 | 0.8437 | 0.8422 |
| $\omega(0.5, 0.5)$ | 1.1726 | — | 1.1744 | 2.0613 | — | 2.0672 |
| $\omega(0.5, 1.0)$ | 6.5631 | 6.5745 | 6.5641 | 14.8036 | 14.8901 | 14.7534 |

### *6.2. Two-dimensional lid-driven flow in a square cavity*

The second test concerns the steady flow of an incompressible viscous fluid in a square cavity where the top wall is driven by a constant velocity $U_0 = 1$. The study of mesh dependence has been conducted for various Reynolds numbers. The errors of the convergence tests are within 2 per cent in terms of the maximum vertical velocity. The result of mesh spacing for various mesh systems are 1/60, 1/120 and 1/240 for $Re = 100$, 400 and 1000 respectively. The Reynolds number is defined as $Re = U_0 L/v$, based on the length of cavity side wall $L$ and the lid-driven velocity $U_0$. The comparison of the values of velocity extrema along the centrelines of the cavity, the vorticity at the centre of the cavity and the vorticity at location $x = 0.5$ on the moving wall, with the numerical results [30,31] for various Reynolds numbers are provided in Table III. The maximum of $ux$ on the vertical line $x = 0.5$ is denoted $ux_{\max}$ and its location is $z_{\max}$. The maximum of $uz$ on the horizontal line $z = 0.5$ is denoted $uz_{\max}$ and its location is $x_{\max}$. Table IV gives the properties of the primary vortex. Finally, in Table V the features of the secondary vortices at the bottom corner are presented. It is clear that the present results are in good agreement with the benchmark results.

The solenoidality constraint of the velocity field is reported in Table VI. The value of maximum $|\nabla \cdot \vec{u}|$ is of the order of about $10^{-12}$ for three values of Reynolds numbers. The accuracy of the present method is thus taken as validated for steady internal flow problems. From the above the treatment is also shown to ensure zero divergence of velocity.

 

Table IV. Comparison of the centre $(x, y)$ of the primary vortex and its streamfunction $\psi$ and vorticity $\omega$.

| | $Re = 100$ | | $Re = 400$ | | $Re = 1000$ | |
|---|---|---|---|---|---|---|
| | Present paper | Reference [30] | Present paper | Reference [30] | Present paper | Reference [30] |
| $\psi$ | −0.1038 | −0.1034 | −0.1141 | −0.1139 | −0.1184 | −0.1179 |
| $\omega$ | 3.1772 | 3.1665 | 2.2955 | 2.2947 | 2.0532 | 2.0497 |
| $x$ | 0.6181 | 0.6172 | 0.5551 | 0.5547 | 0.5321 | 0.5313 |
| $y$ | 0.7352 | 0.7344 | 0.6068 | 0.6055 | 0.5651 | 0.5625 |

Table V. The features of the secondary vortices.

| | $Re = 100$ | | $Re = 400$ | | $Re = 1000$ | |
|---|---|---|---|---|---|---|
| | Present paper | Reference [30] | Present paper | Reference [30] | Present paper | Reference [30] |
| BL | | | | | | |
| $\psi$ | 1.7576e−6 | 1.7488e−6 | 1.4313e−5 | 1.4195e−5 | −2.3349e−4 | 2.3113e−4 |
| $\omega$ | −1.5711e−2 | −1.5551e−2 | −5.7158e−2 | −5.6970e−2 | 0.3529 | −0.3618 |
| $(x, y)$ | (0.0321, 0.0401) | (0.0313, 0.0391) | (0.0512, 0.0491) | (0.0508, 0.0469) | (0.0832, 0.0782) | (0.0859, 0.0781) |
| $(H, V)$ | (0.0811, 0.0811) | (0.0781, 0.0781) | (0.1310, 0.1134) | (0.1273, 0.1081) | (0.2311, 0.1712) | (0.2188, 0.1680) |
| BR | | | | | | |
| $\psi$ | 1.2822e−5 | 1.2537e−5 | 6.4917e−4 | 6.4235e−4 | 1.7286e−3 | 1.7510e−3 |
| $\omega$ | −3.3184e−2 | −3.3075e−2 | −4.3808e−1 | −4.3352e−1 | −1.1211 | −1.1547 |
| $(x, y)$ | (0.9624, 0.0691) | (0.9453, 0.0625) | (0.9003, 0.1276) | (0.8906, 0.1250) | (0.8460, 0.1023) | (0.8594, 0.1094) |
| $(H, V)$ | (0.1351, 0.1527) | (0.1328, 0.1484) | (0.2689, 0.3301) | (0.2617, 0.3203) | (0.2989, 0.3491) | (0.3034, 0.3536) |

BL: bottom left; BR: bottom right.

Table VI. Maximum absolute value of divergence of velocity for two-dimensional lid-driven cavity flows.

| | $Re = 100$ | $Re = 400$ | $Re = 1000$ |
|---|---|---|---|
| $\mathrm{Max}\lvert\nabla \cdot \vec{u}\rvert$ | 1.237e−12 | 3.781e−12 | 6.164e−12 |

### 6.3. *Two-dimensional square driven cavity flow with an oscillating lid*

The unsteady solutions of the driven cavity flow are presented in this section for a simple harmonic oscillation on the top lid. This unsteady driven cavity flow problem has been studied by Soh and Goodrich [32], and more recently, by Iwatsu [33], using different frequencies and Reynolds numbers. In the present simulation, the oscillating lid velocity is given as

$$U(t) = U_0 \sin(\varpi t), \quad \text{at } z = 1 \tag{19}$$

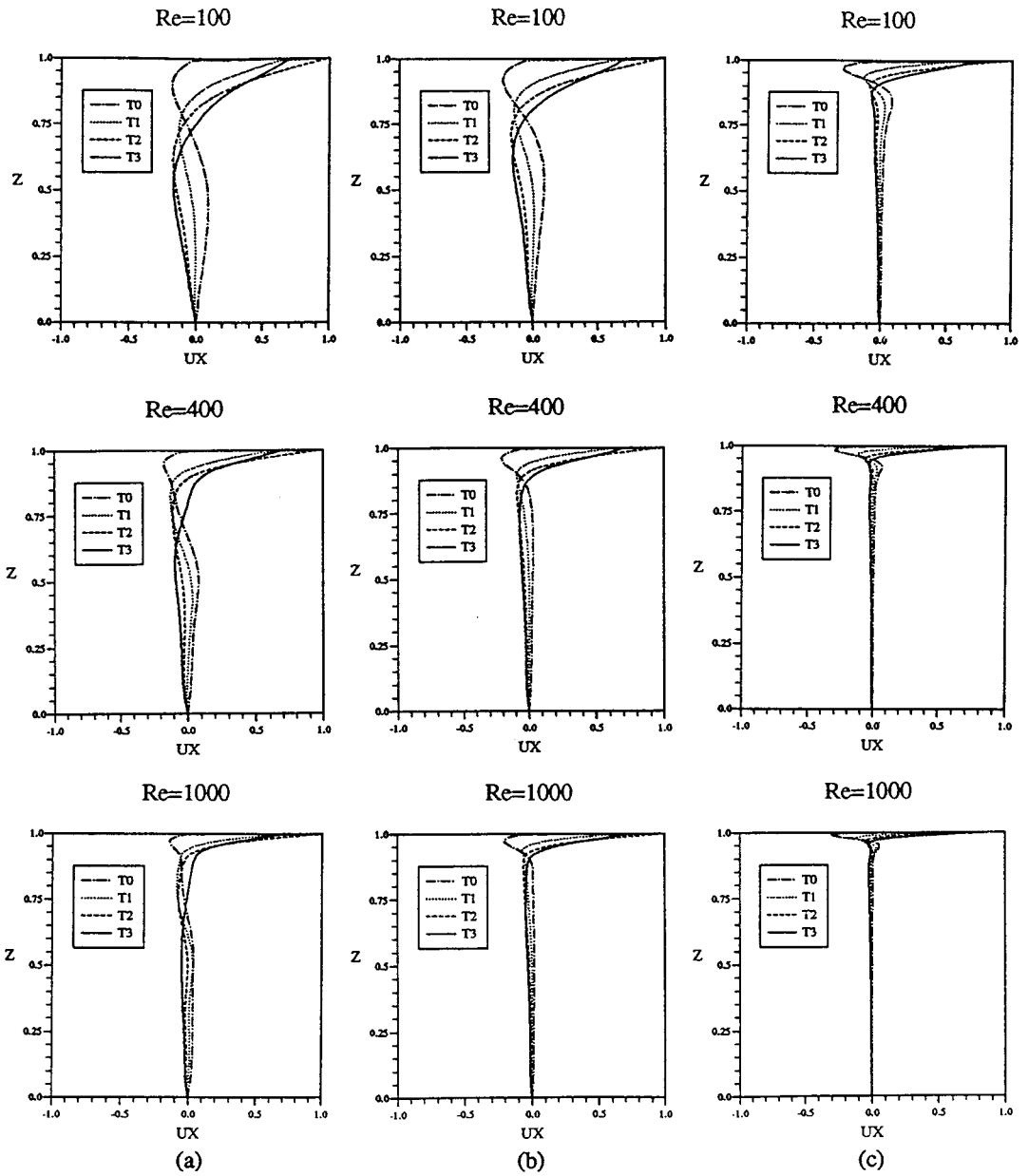


Figure 2. Profiles of $ux$ for the present method along the centreline $x = 0.5$. Times are $T0 = 0$, $T1 = T/8$, $T2 = T/4$, $T3 = 3T/8$; (a) $\varpi = 0.5$, (b) $\varpi = 1$, (c) $\varpi = 10$.

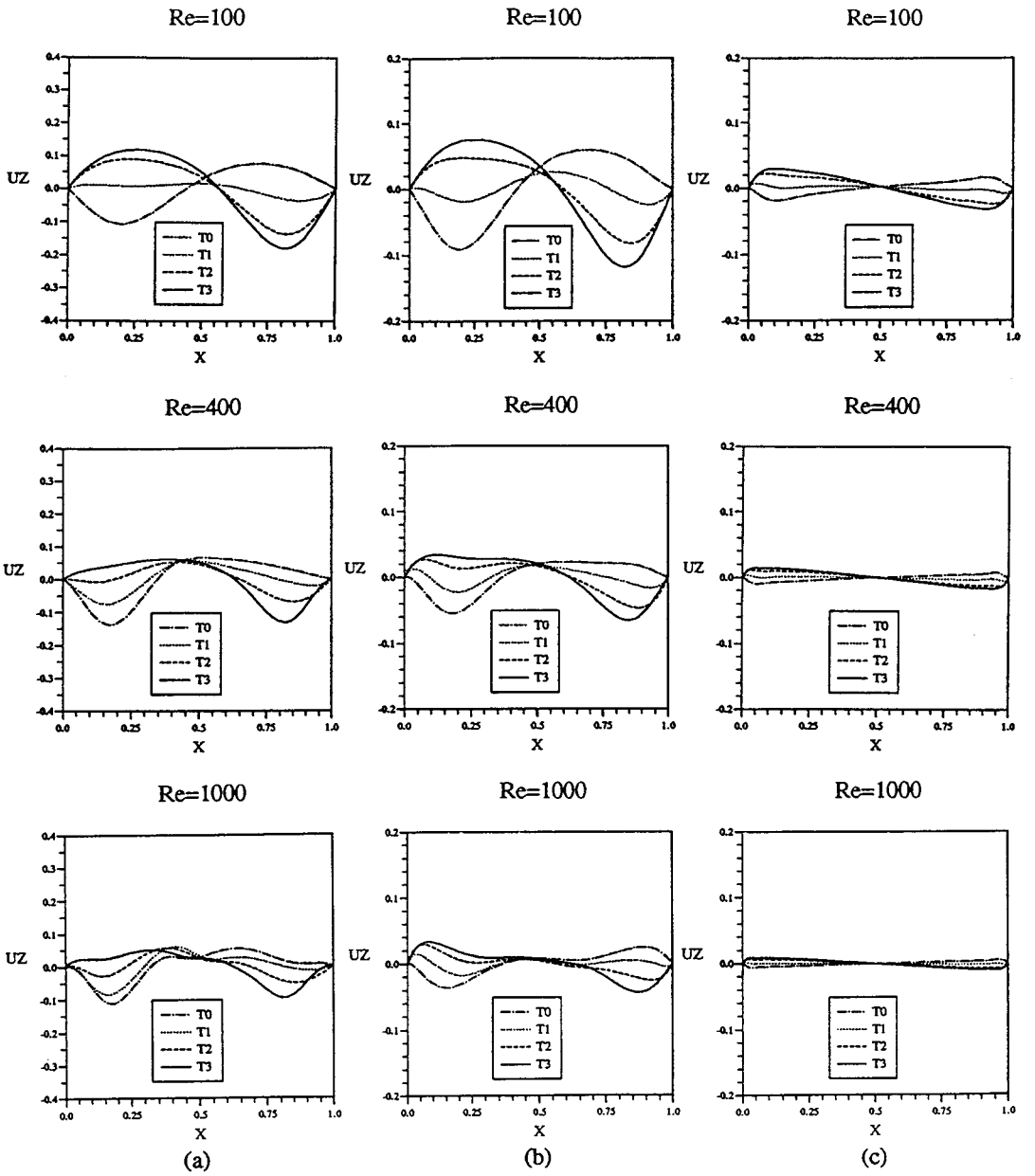


Figure 3. Profiles of $uz$ for the present method along the centreline $z = 0.5$. Times are $T0 = 0$, $T1 = T/8$, $T2 = T/4$, $T3 = 3T/8$; (a) $\varpi = 0.5$, (b) $\varpi = 1$, (c) $\varpi = 10$.

where $\varpi$ is the frequency and the period is $T = 2\pi/\varpi$. The initial condition is $U(0) = 0$ in the computational domain.

Three values of the Reynolds number, $Re = 100$, 400 and 1000, based on the maximum lid velocity $U_0$ and three values of frequencies, $\varpi = 0.5$, 1 and 10, are chosen to investigate this unsteady flow problem. The velocity profiles of the $x$ component along the centreline $x = 0.5$

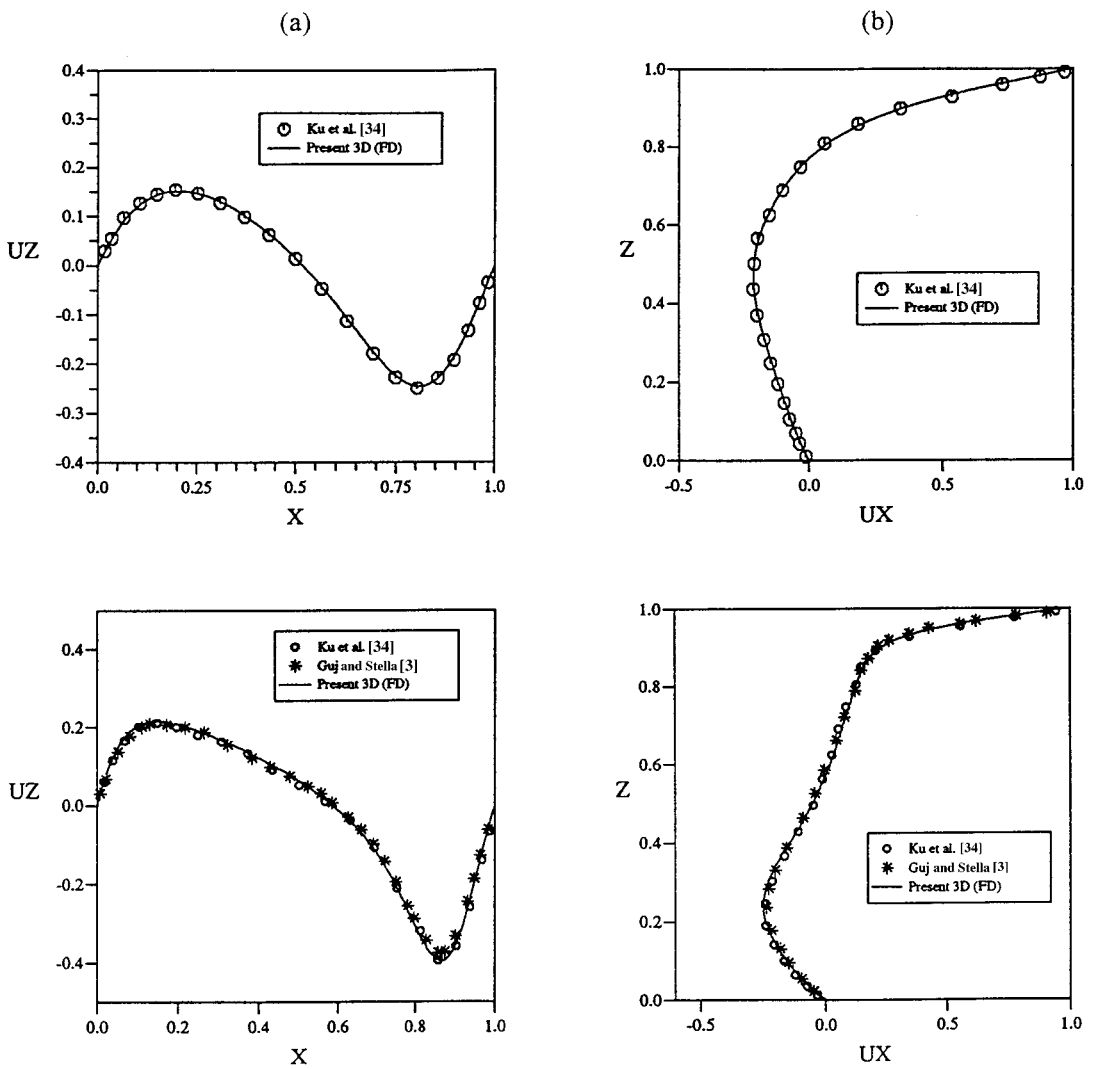


Figure 4. Comparison of the present results with the numerical literatures for (a) $uz$ profile in the horizontal centreline of the plane $z = 0.5$, (b) $ux$ profile in the vertical centreline of the plane $x = 0.5$. Results for $Re = 100$ and 400 are ordered top to bottom.

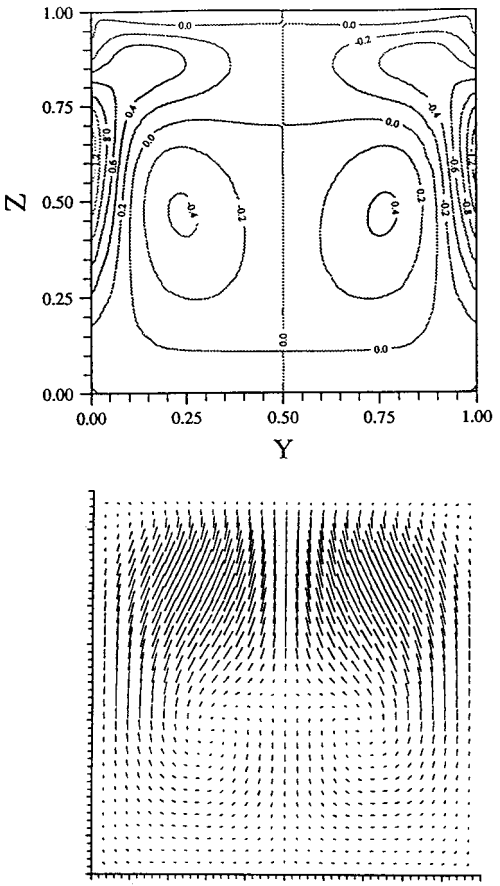


Figure 5. Contour plot of vorticity and vector plot of velocity in the $y$–$z$ plane at $x = 0.5$ for the case of $Re = 100$.

are shown in Figure 2. Comparisons of the present results with those obtained by Iwatsu [33] at $\varpi = 1$ and 10 for $Re = 100$, 400 and 1000, show good agreement.

The $uz$ profiles along the centreline $z = 0.5$ for $Re = 100$, 400 and 1000, with $\varpi = 0.5$, 1.0 and 10.0, are shown in Figure 3. Comparison of Figure 3 with previous results [33] for $\varpi = 1.0$ and 10.0 also show good agreement. The effects of the Reynolds number and the frequency have been studied in Reference [23].

### *6.4. Three-dimensional lid-driven flow in a cubic cavity*

In this section, the steady state solutions of the three-dimensional cubic cavity with an impulsively started lid are presented. This three-dimensional cubic cavity flow problem has been previously studied numerically by a number of people [3,11,34–36]. At present, simulations for the $Re = 100$ and 400 are reported and compared with the results of References [3,34].

 

Computational results for a three-dimensional cavity with an impulsively started lid for $Re = 100$ and 400 are shown in Figures 4–9. Figure 4(a) shows the $uz$ profile on the horizontal centreline of the plane $z = 0.5$ and the $ux$ profile on the vertical centreline of the plane $x = 0.5$ is shown in Figure 4(b). Comparisons made with previous results [3,34] show good agreement for the two Reynolds numbers. The contour plots of vorticity and the vector plots of velocity projected onto the orthogonal mid-planes are shown in Figures 5 and 6 for $Re = 100$ and Figures 7 and 8 for $Re = 400$. For $Re = 100$, only Ku *et al.* [34] showed the vector plots. The comparison of the position of the vortex core in the $y$–$z$ plane at $x = 0.5$ is listed in Table VII. The results show good agreement for the position of the vortex core on the $y$–$z$ plane at $x = 0.5$ for both $Re = 100$ and 400. When the Reynolds number is 400, the secondary flow can be visualized from the vector in the $x$–$y$ plane at $z = 0.5$ in Figure 8, but in Figure 6 (i.e. $Re = 100$), no noticeable secondary flow can be found.

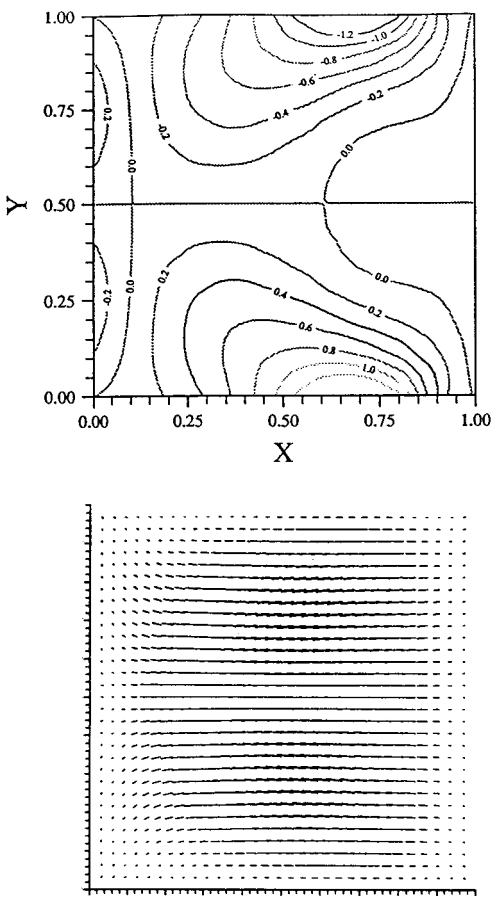


Figure 6. Contour plot of vorticity and vector plot of velocity in the $x$–$y$ plane at $z = 0.5$ for the case of $Re = 100$.

 

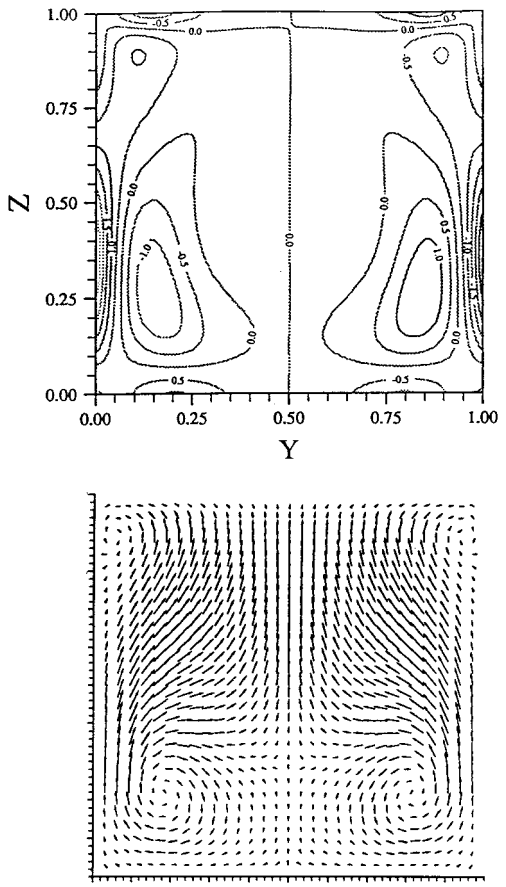


Figure 7. Contour plot of vorticity and vector plot of velocity in the $y$–$z$ plane at $x = 0.5$ for the case of $Re = 400$.

The vorticity contours of the present results are compared with the results of Dacles and Hafez [35] for $Re = 100$ only and with Guevremont *et al.* [36], who used a finite element method to solve the Navier–Stokes equations by a velocity–vorticity formulation for $Re = 100$ and 400. Comparisons made with References [35,36] also show good agreement of the vorticity contours on the three mid-planes at $Re = 100$ and 400.

For the numerical results presented above, the zero divergence of the vorticity field is enforced by replacing the vorticity at each time step with $\nabla \wedge \vec{u}$. To examine the effect of not ensuring zero divergence of vorticity, we run the same case as above without replacing the vorticity with $\nabla \wedge \vec{u}$. Figure 9 shows the velocity profile at the mid-planes for $Re = 100$ and 400. The results for the velocity profile at the mid-planes for $Re = 100$ are not affected by a non-zero divergence, while the case of $Re = 400$ show some differences. In comparison with

 

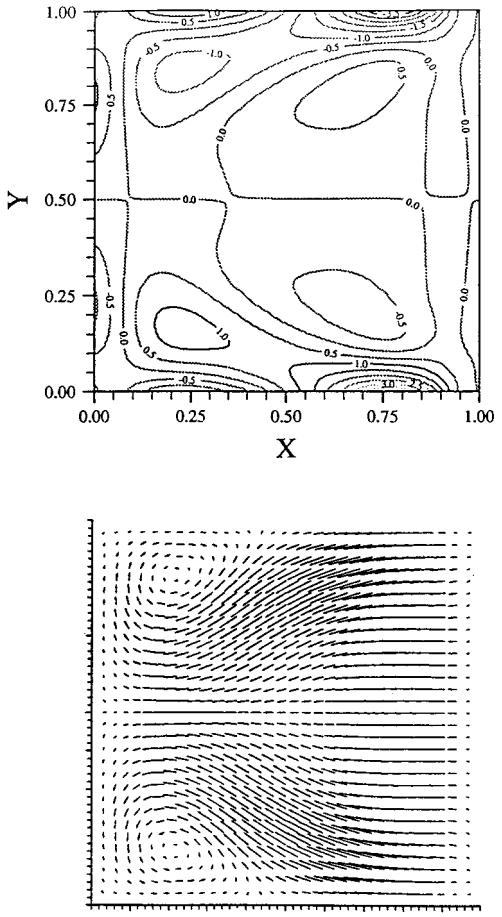


Figure 8. Contour plot of vorticity and vector plot of velocity in the $x$–$y$ plane at $z = 0.5$ for the case of $Re = 400$.

previous results, however, the results obtained by ensuring zero divergence of vorticity are more accurate.

The values of maximum $|\nabla \cdot \vec{u}|$ and $|\nabla \cdot \vec{\omega}|$ for $Re = 100$ and 400 are presented in Table VIII. It is clear that the divergence free of the velocity and vorticity are also satisfied for three-dimensional flow simulations using the present method.

### *6.5. Three-dimensional cubic driven cavity flow with an oscillating lid*

This unsteady problem has been investigated numerically by Iwatsu *et al.* [37]. In the present simulation, the top lid oscillates in its own plane with an oscillation speed $U = U_0 \cos(\varpi t)$. Only a single value of frequency ($\varpi = 1.0$) is studied for both $Re = 100$ and 400. The $uz$ profile

 

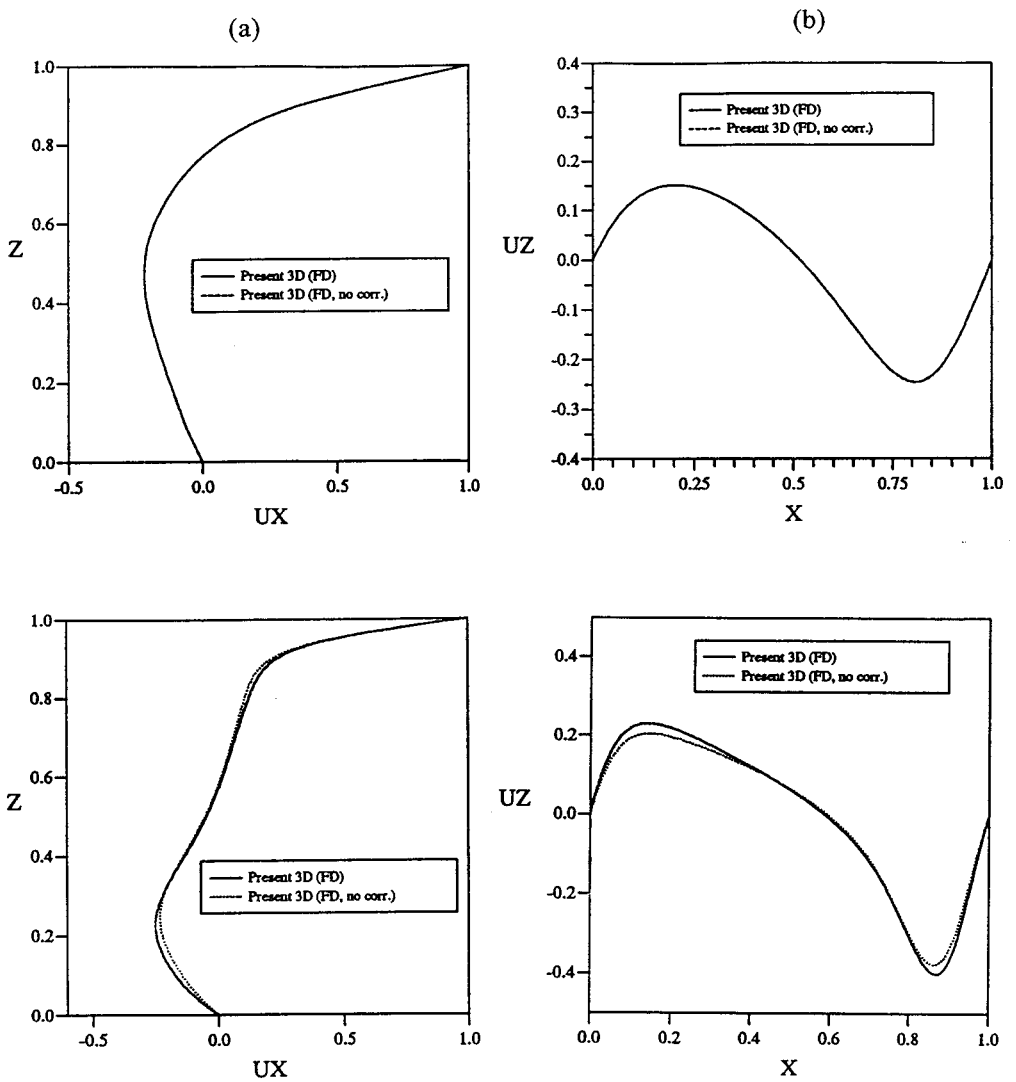


Figure 9. The effect of not ensuring the vorticity has zero divergence for (a) $ux$ profile in the horizontal centreline of the plane $x = 0.5$, (b) $uz$ profile in the vertical centreline of the plane $z = 0.5$. Results for $Re = 100$ and 400 are ordered top to bottom. Dot line showing the vorticity field without using $\nabla \wedge \vec{u}$ to enforce zero divergence.

on the horizontal centreline of the plane $z = 0.5$ and the $ux$ profile on the vertical centreline of the plane $x = 0.5$ are shown in Figure 10(a) and (b) respectively. When the Reynolds number is low, the influence of the top lid motion penetrates deep into the cavity interior (Figure 10(b))

 

Table VII. Comparison of the location of the vortex core for three-dimensional lid-driven cavity flows in the $y$–$z$ plane at $x = 0.5$.

| | $Re = 100$ | | $Re = 400$ | | |
|---|---|---|---|---|---|
| | Present paper | Reference [34] | Present paper | Reference [3] | Reference [34] |
| $x$ | 0.5 | 0.5 | 0.5 | 0.5 | 0.5 |
| $y$ | 0.297 | 0.30 | 0.175 | 0.197 | 0.172 |
| $z$ | 0.36 | 0.36 | 0.221 | 0.227 | 0.220 |

Table VIII. Maximum absolute value of divergence of velocity and vorticity for three-dimensional lid-driven cavity flows.

| | $Re = 100$ | $Re = 400$ |
|---|---|---|
| $\mathrm{Max}\lvert\nabla \cdot \vec{u}\rvert$ | 5.726e−12 | 7.314e−12 |
| $\mathrm{Max}\lvert\nabla \cdot \vec{\omega}\rvert$ | 8.658e−12 | 9.521e−12 |

and this phenomenon can be explained by Figure 10(a), since the $uz$ profile has a larger value at the low Reynolds number. The effect of the Reynolds number on the depth of penetration is similar to the two-dimensional case [33].

The vector plots of velocity projected onto the mid-planes at $y = 0.5$ are shown in Figure 11 for $Re = 400$. The contour plots of vorticity projected onto the orthogonal mid-planes at $y = 0.5$ are shown in Figure 12 for $Re = 400$. Because the two-dimensional results can be compared with the three-dimensional ones by cutting the element cube with a mid-plane on the $y$-axis (i.e. the $x$–$z$ plane at $y = 0.5$), we compare the present results with two-dimensional solutions from a previous study [33]. Since the oscillation of the top lid is describable by a cosine function in the three-dimensional simulation, we can shift the time period of the two-dimensional case by adding a value of $T/4$. Therefore, the vector plots of velocity in the $x$–$z$ plane at $y = 0.5$ from $t = 0$ to $3T/8$ with an increasing times by $T/8$ correspond to the two-dimensional case with time from $T/4$ to $5T/8$ [33]. In summary, the results show that the behaviour of the three-dimensional flow on the symmetry plane is qualitatively similar to that of the results of two-dimensional computations. From this comparison, the vector plots of velocity on the $x$–$z$ plane at $y = 0.5$ are qualitatively similar to the two-dimensional case. Comparison of the vector plots of velocity on the $x$–$z$ plane at $y = 0.5$ for the case of $Re = 400$ with Reference [37] at times $T/4$, $3T/8$, $T/2$ and $5T/8$ also shows good qualitative agreement. Therefore, the above comparisons demonstrate that the three-dimensional cavity interior (on the $x$–$z$ plane at $y = 0.5$) has the feature of qualitative resemblance to the two-dimensional case.

 

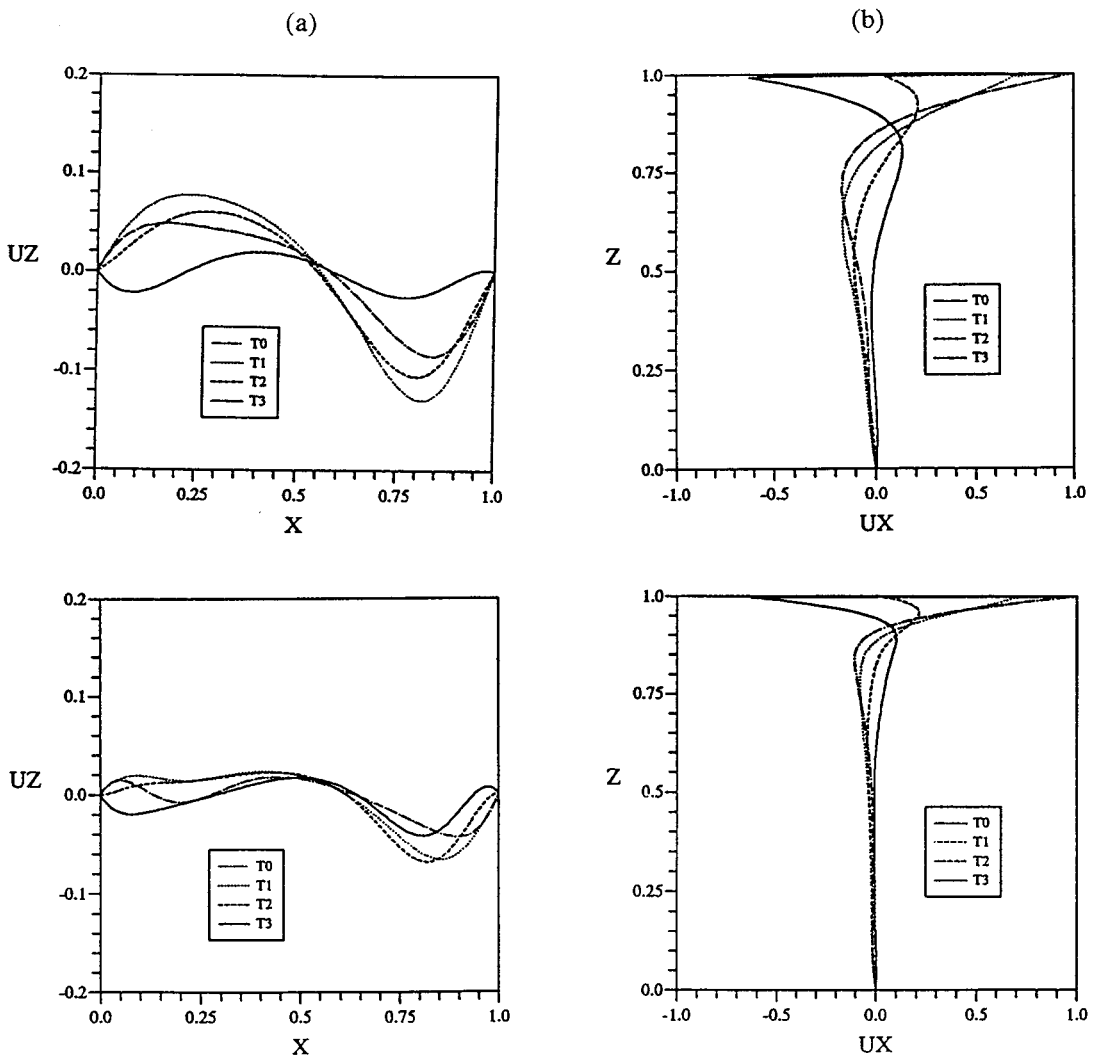


Figure 10. (a) $uz$ profile in the horizontal centreline of the plane $z = 0.5$, (b) $ux$ profile in the vertical centreline of the plane $x = 0.5$. Times are $T0 = 0$, $T1 = T/8$, $T2 = T/4$, $T3 = 3T/8$. Results for $Re = 100$ and 400 are ordered top to bottom.

## 7. CONCLUSIONS

A velocity–vorticity finite difference method is developed to solve the incompressible viscous steady and unsteady two- and three-dimensional flow problems. All variables of the method are placed on a staggered mesh and a proper treatment of boundary conditions is employed to

 

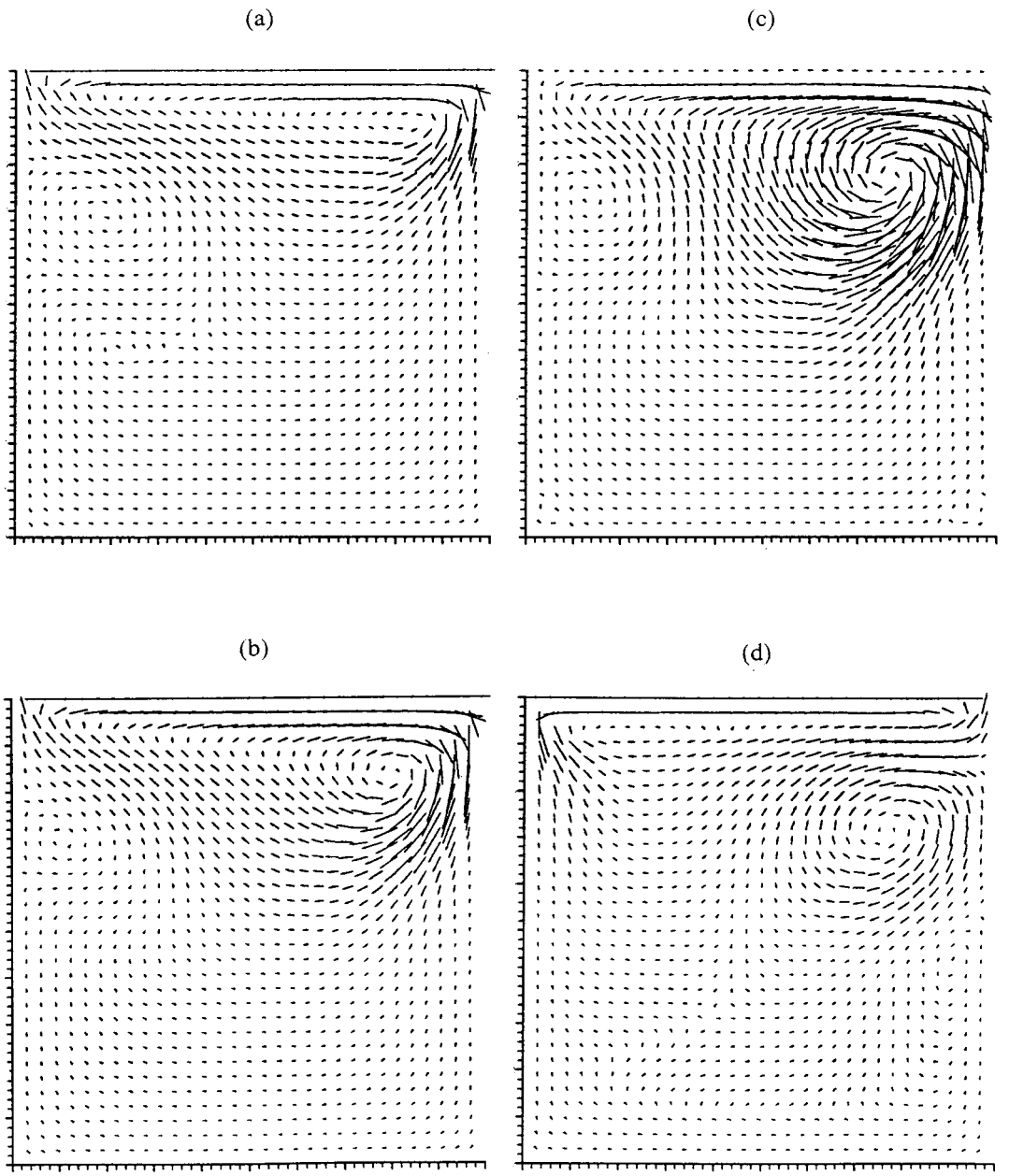


Figure 11. Time sequence of the velocity vector plots in the $x$–$z$ plane at $y = 0.5$ for the case of $Re = 400$. Times shown are (a) $t = 0$, (b) $t = T/8$, (c) $t = T/4$, (d) $t = 3T/8$.

satisfy the zero divergence of the velocity field. To enforce the zero divergence of the vorticity, the computed vorticity was replaced at each time step with $\nabla \wedge \vec{u}$. Both steady and unsteady computations using the present method of solution have been compared with the numerical

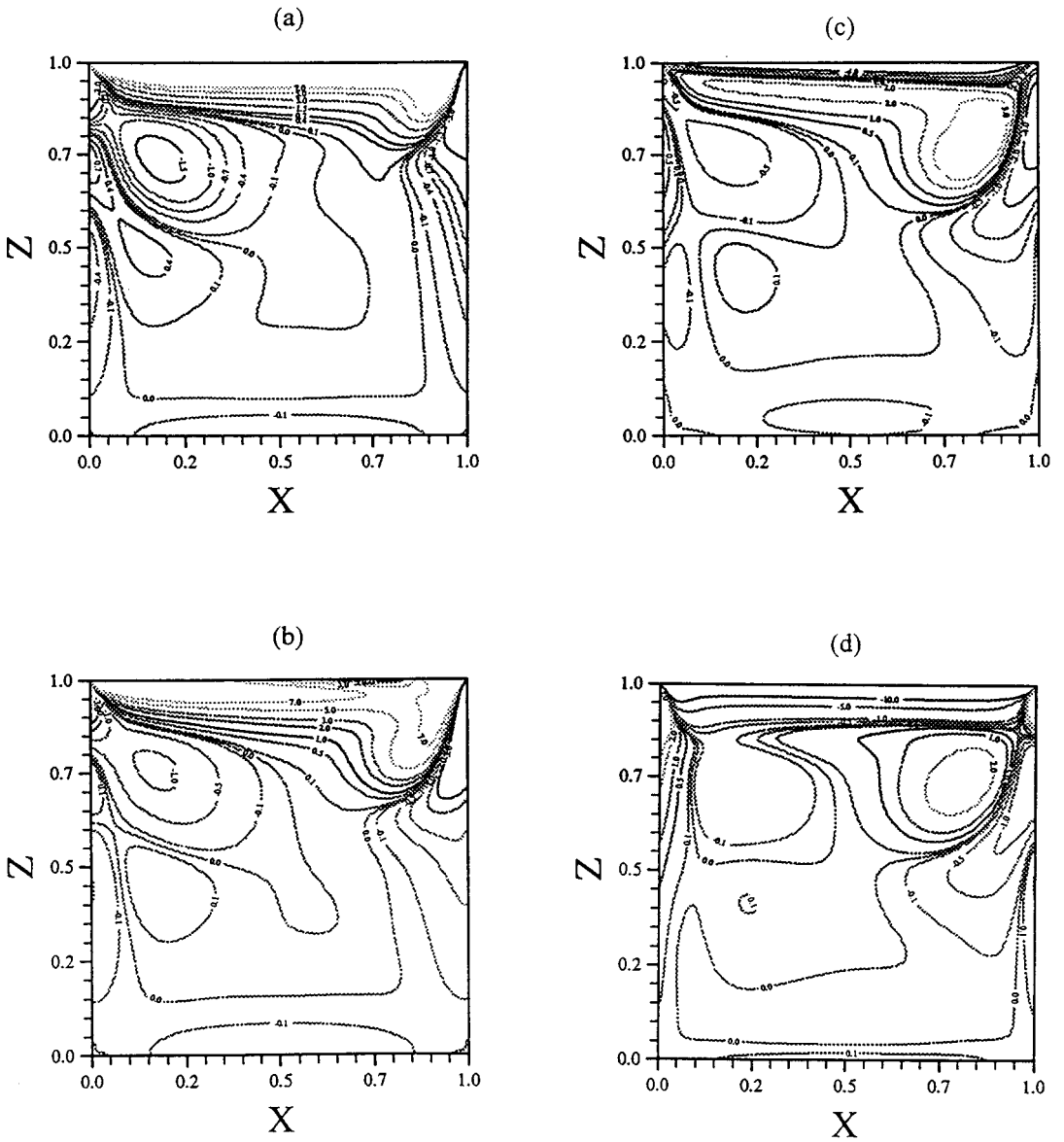


Figure 12. Time sequence of the vorticity contour plots in the $x$–$z$ plane at $y = 0.5$ for the case of $Re = 400$. Times shown are (a) $t = 0$, (b) $t = T/8$, (c) $t = T/4$, (d) $t = 3T/8$.

literature at various Reynolds numbers. The present method produces accurate results as shown by these comparisons. It was, however, shown that without enforcing the zero divergence of vorticity, small inaccurate results were observed with progressively larger errors as Reynolds number increases.

The present method could serve as a base for further studies on the three-dimensional vortex particle method.

## ACKNOWLEDGMENTS

The author gratefully acknowledges Dr. D. J. Doorly for many helpful discussions. This work was supported financially by the National Science Council of the Republic of China under Grand NSC-87-2212-E-014-020. The comments of the referee and editor are appreciated.

## REFERENCES

1. Kim J, Moin M. Application of a fraction-step method of incompressible Navier–Stokes equations. *Journal of Computational Physics* 1985; **59**: 308–323.
2. Wong AK, Retzes JA. An effective vorticity–vector potential formulation for the numerical solutions of three-dimensional duct flow problems. *Journal of Computational Physics* 1984; **55**: 353–383.
3. Guj G, Stella A. A vorticity–velocity method for the numerical solution of 3D incompressible flows. *Journal of Computational Physics* 1993; **106**: 286–298.
4. Gresho PM. Incompressible fluid dynamics: some fundamental formulation issues. *Annual Review of Fluid Mechanics* 1991; **23**: 413–453.
5. Speziale CG. On the advantages of the vorticity–velocity formulation of the equation of fluid dynamics. *Journal of Computational Physics* 1987; **73**: 476–480.
6. Gatski TB, Grosh CE, Rose ME. A numerical study of the two-dimensional Navier–Stokes equations in vorticity–velocity variables. *Journal of Computational Physics* 1982; **48**: 1–22.
7. Gatski TB, Grosch CE. Embeded cavity drag in steady laminar flows. *AIAA Journal* 1985; **23**: 1028–1037.
8. Gatski TB, Grosch CE, Rose ME. The numerical solution of the Navier–Stokes equations for three-dimensional unsteady incompressible flows by compact schemes. *Journal of Computational Physics* 1989; **82**: 298–329.
9. Fasel H. Investigation of the stability of the boundary layers by a finite difference model of the Navier–Stokes equations. *Journal of Fluid Mechanics* 1976; **78**: 355–383.
10. Fasel H, Rist U, Konezelmann U. Numerical investigation of the three dimensional development in boundary layer transition. *AIAA Journal* 1990; **28**: 29–37.
11. Dennis SCR, Ingham DB, Cook RN. Finite difference methods for calculating steady incompressible flows in three-dimensions. *Journal of Computational Physics* 1979; **33**: 325–329.
12. Farouk B, Fusegi T. A coupled solution of the vorticity–velocity formulation of the incompressible Navier–Stokes equations. *International Journal for Numerical Methods in Fluids* 1985; **5**: 1017–1034.
13. Orlandi P. Vorticity–velocity formulation for high *Re* flows. *Computers and Fluids* 1987; **7**: 137–149.
14. Guj G, Stella A. Numerical solutions of high-Re recirculating flows in vorticity–velocity form. *International Journal for Numerical Methods in Fluids* 1988; **8**: 405–416.
15. Ern A, Smooke MD. Vorticity–velocity formulation for three dimensional steady compressible flows. *Journal of Computational Physics* 1993; **105**: 58–71.
16. Yuan L, Fu D, Ma Y. Numerical solution of axisymmetric unsteady incompressible flow by a vorticity–velocity method. *International Journal for Numerical Methods in Fluids* 1995; **21**: 401–411.
17. Stella F, Bucchignani E. True transient vorticity–velocity method using preconditioned Bi-CGSTAB. *Numerical Heat Transfer B* 1996; **30**: 315–339.
18. Huang H, Li M. Finite-difference approximation for the velocity–vorticity formulation on staggered and non-staggered grids. *Computers and Fluids* 1997; **26**: 59–82.
19. Pascazio G, Napolitano M. A staggered-grid finite volume method for the vorticity–velocity equations. *Computers and Fluids* 1996; **25**: 433–446.
20. Shen W, Loc T. Numerical method for unsteady 3D Navier–Stokes equations in velocity–vorticity form. *Computers and Fluids* 1997; **26**: 193–216.
21. Daube O. Resolution of the 2D Navier–Stokes equations in velocity–vorticity form by means of an influence matrix technique. *Journal of Computational Physics* 1992; **103**: 402–414.

 

22. Cottet GH. Boundary conditions and the deterministic vortex methods for the Navier–Stokes equations. In *Mathematical Aspects of Vortex Dynamics*, Caflish RE (ed.). SIAM: Philadelphia, PA, 1988; 128–143.
23. Liu CH, Doorly DJ. Velocity–vorticity formulation with vortex particle-in-cell method for incompressible viscous flow simulation, part I: formulation and validation. *Numerical Heat Transfer B* 1999; **35**: 251–275.
24. Liu CH, Doorly DJ. Velocity–vorticity formulation with vortex particle-in-cell method for incompressible viscous flow simulation, part II: application to vortex/wall interactions. *Numerical Heat Transfer B* 1999; **35**: 277–294.
25. Leonard BP. A stable and accurate convective modelling procedure based on quadratic upstream interpolation. *Computer Methods in Applied Mechanics and Engineering* 1979; **19**: 59–98.
26. Peyret R, Taylor TD. *Computational Methods for Fluid Flow*. Springer: New York, 1983.
27. Saad Y, Schultz MH. GMRES: a generalized minimal residual algorithm for solving nonsymmetric linear systems. *SIAM Journal of Scientific and Statistical Computing* 1986; **7**: 856–869.
28. Gustafsson I. A class of first order factorization methods. *BIT* 1978; **18**: 142–156.
29. Eisenstat SC. Efficient implementation of a class of preconditioned conjugate gradient methods. *SIAM Journal of Scientific and Statistical Computing* 1981; **2**: 1–4.
30. Ghia U, Ghia KN, Shin CT. High-resolutions for incompressible flow using the Navier–Stokes equations and a multigrid method. *Journal of Computational Physics* 1982; **48**: 387–411.
31. Botella O, Peyret R. Benchmark spectral results on the lid-driven cavity flow. *Computers and Fluids* 1988; **27**: 421–433.
32. Soh WY, Goodrich JW. Unsteady solution of incompressible Navier–Skokes equations. *Journal of Computational Physics* 1988; **79**: 113–134.
33. Iwatsu R, Hyun JM, Kuwahara K. Numerical simulation of flows driven by a torsionally oscillating lid in a square cavity. *Journal of Fluids and Engineering* 1992; **114**: 143–151.
34. Ku HC, Hirsh RS, Taylor T. A pseudospectral method for solution of the three-dimensional incompressible Navier–Stokes equations. *Journal of Computational Physics* 1987; **70**: 439–462.
35. Dacles J, Hafez M. Numerical methods for 3-D viscous incompressible flows using a velocity/vorticity formulation. AIAA Paper No. 90-0237, 1990.
36. Guevremont G, Habashi WG, Kotiuga PL, Hafez M. Finite element solution of the 3D compressible Navier–Stokes equations by a velocity–vorticity method. *Journal of Computational Physics* 1993; **107**: 176–187.
37. Iwatsu R, Hyun JM, Kuwahara K. Numerical simulation of three-dimensional flows in a cubic box with an oscillating lid. *Journal of Fluids and Engineering* 1993; **115**: 680–686.

 